

**FORMATION OF CERIA BUFFER LAYER FOR  
YBa<sub>2</sub>Cu<sub>3</sub>O<sub>7-x</sub> SUPERCONDUCTORS**

**LIM SHU LEE**

**UNIVERSITI SAINS MALAYSIA**

**2010**

**FORMATION OF CERIA BUFFER LAYER FOR  $\text{YBa}_2\text{Cu}_3\text{O}_{7-x}$   
SUPERCONDUCTORS**

**by**

**LIM SHU LEE**

**Thesis submitted in fulfilment of the requirements**

**for the degree of**

**Masters of Science**

**October 2010**

## ACKNOWLEDGEMENTS

Foremost, I would like to express my deep and sincere gratitude to my principal supervisor Assoc. Prof. Dr. Zainovia Lockman for the continuous support of my research study since my undergraduate, for her guidance, enthusiasm and immense knowledge. Her great efforts to explain things clearly and simply helped me in all the time of research and writing of this thesis. I also would like to express my honour gratitude to my co-supervisor, Prof. Zainal Arifin Ahmad for his detailed and constructive comments.

I wish to express my warm and sincere thanks to all academic, administration and technical staffs of the School of Materials and Mineral Resources Engineering (SMMRE) for the endless support and help. I also extend my thanks to all my group members particularly Normi Akmal Mustaffa, Tan Wai Kian, Syahrizal Ismail and Leow Cheah Li for the friendship and team work. Besides that, I would like to thank Dr. Khairunisak Abdul Razak for the unreserved help and support.

My sincere gratitude goes to Prof. Atsunori Matsuda from Department of Materials Science, Toyohashi University of Technology who gave me the opportunity to work in his lab during my research attachment for 11 months in Japan. Apart from that, many thanks to Assoc. Prof Jun-ichi Hamagami, Dr. Go Kawamura, Assoc. Prof. Hiroyuki Muto and Prof. Mototsugu Sakai for the valuable help and unreserved support. Apart from that, the assistance and friendship from all the members of Sakai-Matsuda lab are very much appreciated. Special thanks to

Hiroyuki Oda, Niki Prastomo, Pascal Sugri, Akihiro Mitani, Hisatoshi Sakamoto and Mohamad Arif for the guidance in the handling of equipments and data analysis.

I am deeply grateful to my beloved parents Lim Yak Hoon and Khaw Mooi Im for supporting me spiritually throughout my life. Warm thanks also to all my friends for the kindness and encouragement.

Last but not the least, the financial supports from fellowship of University Sains Malaysia, E-Science Fund (account no. 6013332) and JENESYS programme 2009/2010 supported by JASSO are gratefully acknowledged.

## TABLE OF CONTENTS

	<b>Page</b>
<b>ACKNOWLEDGEMENTS</b>	<b>ii</b>
<b>TABLE OF CONTENTS</b>	<b>iv</b>
<b>LIST OF TABLES</b>	<b>viii</b>
<b>LIST OF FIGURES</b>	<b>x</b>
<b>LIST OF ABBREVIATIONS</b>	<b>xx</b>
<b>LIST OF SYMBOLS</b>	<b>xxii</b>
<b>ABSTRAK</b>	<b>xxiii</b>
<b>ABSTRACT</b>	<b>xxv</b>
<b>CHAPTER 1: INTRODUCTUON</b>	
1.1 Introduction	1
1.2 Objectives	2
1.3 Research Motivation	2
1.4 Scope of Investigation	3
1.5 Outline of Chapter	4
<b>CHAPTER 2: LITERATURE REVIEW</b>	
2.1 Introduction	6
2.2 Introduction of Superconductivity	6
2.3 Type I and Type II Superconductors	9
2.4 Cuprate High Temperature Superconductors	12
2.5 Substrate	16
2.5.1 Substrates Requirements for YBCO Coated Conductor	16

2.5.2	Rolling-Assisted-Biaxially-Textured-Substrates (RABITS)	18
	Process	
	2.5.2.1 RABiT Substrate	19
2.5.3	Ion-Beam-Assisted Deposition (IBAD) Process	21
2.5.4	Inclined Substrate Deposition (ISD) Process	22
2.6	Oxide Buffer Layer	23
	2.6.1 Buffer Layer Deposition Techniques	23
	2.6.1.1 Precursors Solution	28
	2.6.1.2 Coating	30
	2.6.1.3 Advantages and Disadvantages of Spin Coating	35
	2.6.2 Annealing	36
2.7	CeO <sub>2</sub> as a Buffer Layer	38
	2.7.1 Deposition of CeO <sub>2</sub> Film for Coated Conductor	40
	2.7.2 CeO <sub>2</sub> on Ni-based Substrates	41
	2.7.3 CeO <sub>2</sub> on Cu-based Substrate	46
2.8	CeO <sub>2</sub> Pinning Centres	49
	2.8.1 YBCO Film Deposition	52
<b>CHAPTER 3: METHODOLOGY</b>		
3.1	Introduction	54
3.2	Substrate	55
3.3	Preparation of Ce Precursor Solution	56
3.4	Spin coating	59
3.5	Annealing	59
3.6	Deposition on RABiT Cu	61

3.7	Characterizations	63
3.7.1	Optical Microscope	64
3.7.2	Field Emission Scanning Electron Microscope	64
3.7.3	Energy Dispersive X-Ray	65
3.7.4	X-Ray Diffraction Spectroscopy	66
3.7.5	Atomic Force Microscopy	67
3.7.6	Thermogravimetric Analyser	68
3.7.7	Raman Spectroscopy	68

## **CHAPTER 4: RESULTS AND DISCUSSION**

4.1	Introduction	69
4.2	Precursor Solution Preparation	70
4.3	Chemical Solution Derived CeO <sub>2</sub> Film	73
4.4	Polycrystalline Ni as Substrate	77
4.4.1	Substrate Preparation	77
4.4.2	Effect of Precursor Solution Concentration	79
4.4.3	Effect of Annealing Temperature	86
4.5	Deposition on RABiT Ni	94
4.5.1	Effect of Annealing Temperature	96
4.5.2	Effect of Annealing Time	103
4.5.3	Effect of Methanol	108
4.5.4	Effect of Acetic Acid as Solvent	113
4.6	Deposition on RABiT Cu	115
4.6.1	Effect of Precursor Solution Concentration	116
4.6.1.1	Layered Oxide Structures Formation on Cu	132

4.6.2	Effect of Annealing Temperature	143
4.6.3	Annealing in Vacuum	150
4.6.3.1	Effect of Precursor Solution Concentration	151
4.6.3.2	Effect of Annealing Temperature	164
4.6.4.3	Effect of Annealing Time	168
 <b>CHAPTER 5: CONCLUSIONS AND RECOMMENDATION</b>		
5.1	Introduction	173
5.2	Conclusions	174
5.3	Recommendations for Future Development	177
 <b>REFERENCES</b>		
		179
 <b>APPENDICES</b>		
Appendix A: ICDD Number		



## LIST OF TABLES

		<b>Page</b>
Table 2.1	Example of Type I and Type II low temperature superconductors and their $T_c$ values.	10
Table 2.2	Example of cuprate HTS with their $T_c$ and $J_c$ at zero field.	12
Table 2.3	Properties of some commonly used metallic RABiT substrates.	21
Table 2.4	Buffer layer deposition methods and their respective definition.	24
Table 2.5	Summary of methods used to deposit buffer layers in recent years and the related authors.	26
Table 2.6	Physical properties of $CeO_2$ .	39
Table 2.7	Summary of works for CSD derived $CeO_2$ film on RABiT Ni substrate and the related authors.	45
Table 3.1	Summary of solution concentrations used for deposition on Ni-based substrates (annealed in Ar-5% $H_2$ at 1000°C for 1 h).	58
Table 3.2	Summary of volume % methanol used in the Ce precursor solution for deposition on RABiT Ni (annealed in Ar-5% $H_2$ at 1000°C for 1 h).	59
Table 3.3	Summary of different temperature used for annealing in Ar-5% $H_2$ for the film deposited on RABiT Ni.	60
Table 3.4	Summary of different time used for annealing in Ar-5% $H_2$ for the film deposited on RABiT Ni.	60
Table 3.5	Concentration of Ce precursor solution studied for the $CeO_2$ formation on RABiT Cu (annealed in Ar-5% $H_2$ at 1000°C for 1 h).	62

Table 3.6	Conditions of annealing temperature and annealing time studied for the CeO <sub>2</sub> formation on RABiT Cu (annealed in Ar-5%H <sub>2</sub> ).	62
Table 3.7	Concentration of Ce precursor solution studied for the CeO <sub>2</sub> formation on RABiT Cu (annealed in vacuum at 1000°C for 1 h).	63
Table 3.8	Conditions of annealing temperature and annealing time studied for the CeO <sub>2</sub> formation on RABiT Cu (annealed in vacuum).	63
Table 3.9	ICDD numbers used for characterization of phases.	67
Table 4.1	Summary of the observations and findings for the investigation of concentration of Ce precursor solutions. All samples were annealed at 1000°C for 1 h under Ar-5%H <sub>2</sub> .	79
Table 4.2	Summary of the observations and findings for the investigation of coatings produced from 0.30 mol/l solution and being annealed at different temperatures (800 to 1100°C) for 1 h in Ar-5%H <sub>2</sub> .	86
Table 4.3	Summary of the observations and findings for the investigation of annealing temperature on the spin coated RABiT Ni.	96
Table 4.4	Summary of the observations and findings from XRD patterns for coating produced at 1000°C in Ar-5%H <sub>2</sub> for different annealing time.	104
Table 4.5	Summary of the observations and findings for the investigation of the addition of different volume % methanol to adjust the concentration of Ce precursor solution to 0.30 mol/l (annealed at 1000°C for 1 h in Ar-5%H <sub>2</sub> ).	109
Table 4.6	Summary of observations for coatings formed on RABiT Cu deposited with different concentrations of Ce precursor solution (annealed at 1000°C for 1 h in Ar-5%H <sub>2</sub> ).	117
Table 4.7	$\Delta G^{\circ}_T$ for the formation of CuO, Cu <sub>2</sub> O and CeO <sub>2</sub> at 1273 K as taken from the graph in Figure 4.54.	133

## LIST OF FIGURES

		<b>Page</b>
Figure 2.1	Temperature dependence of electrical resistivity of a superconductor.	7
Figure 2.2	Meissner effect for Type I superconductor.	8
Figure 2.3	Magnetization (M) as the function of applied magnetic field for (a) Type I and (b) Type II superconductors.	10
Figure 2.4	Typical architecture of YBCO coated conductor.	14
Figure 2.5	(a) YBCO grains grow on buffered textured substrate with low angle grain boundaries, (b) crystal structure of YBCO.	14
Figure 2.6	Schematic illustration of textured substrate preparation method using RABiTS process.	19
Figure 2.7	Schematic illustration of IBAD process.	22
Figure 2.8	Schematic illustration of ISD process.	23
Figure 2.9	Flow chart of a typical CSD method for the formation of crystallized film.	27
Figure 2.10	Four commonly used coating techniques for CSD process.	31
Figure 2.11	Four stages of spin coating: (a) deposition, (b) spin up, (c) spin off and (d) evaporation.	35
Figure 2.12	Illustration of cubic fluorite structure of CeO <sub>2</sub> .	39
Figure 2.13	Three stack oxide buffer layers in 2G coated conductors: CeO <sub>2</sub> /YSZ/Y <sub>2</sub> O <sub>3</sub> buffer layers as used by American Superconductor Corporation Inc.	40
Figure 2.14	Transportation of J leads to a F moving the vortex lattice across the HTS material, resulting a low J <sub>c</sub> .	52
Figure 3.1	Flow chart of preparation of Ce precursor solution with cerium(III) acetate, acetic acid or propionic acid and methanol as starting materials.	57

Figure 4.1	Photographs of precursor solution using (a) cerium(III) acetate dissolved in propionic acid and methanol, and (b) cerium(III) acetate dissolved in acetic acid and methanol.	71
Figure 4.2	TGA curve of $\text{Ce}(\text{CH}_3\text{CO}_2)_3 \cdot x\text{H}_2\text{O}$ from room temperature to $1000^\circ\text{C}$ in air.	71
Figure 4.3	Three stages in CSD process and the factors that may affect the quality of film in each stage.	73
Figure 4.4	Schematic illustrations for the formation of CSD derived film on textured metallic substrate.	74
Figure 4.5	Schematic diagram of the free energies of a CSD derived amorphous film, the ideal supercooled film and a crystalline phase.	76
Figure 4.6	Optical microscope images of polycrystalline Ni substrate (a) as received (b) after polishing and 2 min of etching (images = 50 KX).	78
Figure 4.7	XRD pattern of the polycrystalline Ni substrate before deposition of $\text{CeO}_2$ film.	78
Figure 4.8	Surface morphologies of coatings on polycrystalline Ni substrates after annealed at $1000^\circ\text{C}$ in Ar-5% $\text{H}_2$ for 1 h, deposited from (a) 0.10 mol/l, (b) 0.20 mol/l, (c) 0.30 mol/l and (c) 0.40 mol/l Ce precursor solution respectively.	80
Figure 4.9	(a) 2D and (b) 3D AFM images of coating on polycrystalline Ni substrate after annealed at $1000^\circ\text{C}$ in Ar-5% $\text{H}_2$ for 1 h, deposited from 0.30 mol/l Ce precursor solution.	82
Figure 4.10	EDX measurement for coating produced from 0.10 mol/l solution after being annealed at $1000^\circ\text{C}$ for 1 h in Ar-5% $\text{H}_2$ . (a) SEM morphology, (b) table for element in at% for point A and B.	83
Figure 4.11	EDX measurement for coating produced from 0.20 mol/l solution after being annealed at $1000^\circ\text{C}$ for 1 h in Ar-5% $\text{H}_2$ . (a) SEM morphology, (b) table for element in at% for point A and B.	83
Figure 4.12	EDX measurement for coating produced from 0.30 mol/l solution after being annealed at $1000^\circ\text{C}$ for 1 h in Ar-5% $\text{H}_2$ . (a) Surface morphology measured, (b) table for element in at% for whole area.	84

Figure 4.13	EDX measurement for coating produced from 0.40 mol/l solution after being annealed at 1000°C for 1 h in Ar-5%H <sub>2</sub> . (a) Surface morphology measured, (b) table for element in at% for point A.	84
Figure 4.14	FESEM images of cracked coating on polycrystalline Ni substrate (tilted at 45°) produced from (a) 0.10 mol/l and (b) 0.20 mol/l Ce precursor solutions respectively after being annealed at 1000°C for 1 h in Ar-5%H <sub>2</sub> .	85
Figure 4.15	XRD patterns of coatings produced from different concentration of Ce precursor solution (as listed) after being annealed at 1000°C for 1 h in Ar-5%H <sub>2</sub> .	85
Figure 4.16	Surface morphologies of coatings on polycrystalline Ni substrates, produced from 0.30 mol/l Ce precursor solution and annealed for 1 h in Ar-5%H <sub>2</sub> at (a) 800°C, (b) 900°C, (c) 1000°C and (d) 1100 °C respectively.	87
Figure 4.17	2D AFM images of coatings on polycrystalline Ni substrates, produced using 0.30 mol/l Ce precursor solution and annealed for 1 h in Ar-5%H <sub>2</sub> at (a) 800°C, (b) 900°C and (c) 1000°C respectively.	89
Figure 4.18	EDX measurement of coating on polycrystalline Ni substrate annealed for 1 h in Ar-5%H <sub>2</sub> at 800°C. (a) Surface morphology measured, (b) table for element in at%.	89
Figure 4.19	EDX measurement of coating on polycrystalline Ni substrate annealed for 1 h in Ar-5%H <sub>2</sub> at 900°C. (a) Surface morphology measured, (b) table for element in at%.	90
Figure 4.20	EDX measurement of coating on polycrystalline Ni substrate annealed for 1 h in Ar-5%H <sub>2</sub> at 1100°C. (a) SEM morphology, (b) table for element in at% for point A and B.	90
Figure 4.21	FESEM images of 45° tilt samples produced using 0.30 mol/l Ce precursor solution and annealed at (a) 900 and (b) 1100°C respectively for 1 h in Ar-5%H <sub>2</sub> .	91
Figure 4.22	XRD patterns of the coatings produced from 0.30 mol/l solution after being annealed at (a) 800°C, (b) 900°C and (c) 1100°C for 1 h under Ar-5%H <sub>2</sub> .	91
Figure 4.23	Schematic diagram of the formation of particle-like structure of coating if the sample is subjected to high annealing temperature.	94

Figure 4.24	(a) Surface morphology and (b) XRD pattern for RABiT Ni substrate used for CeO <sub>2</sub> deposition.	95
Figure 4.25	Surface morphologies of coatings on RABiT Ni produced using 0.30 mol/l Ce precursor solution and annealed for 1 h in Ar-5%H <sub>2</sub> at (a) 800°C, (b) 900°C, (c) 1000°C and (d) 1100°C respectively.	97
Figure 4.26	2D images of AFM for coatings on RABiT Ni produced using 0.30 mol/l Ce precursor solution and annealed for 1 h in Ar-5%H <sub>2</sub> at (a) 800°C, (b) 900°C and (c) 1000°C respectively.	98
Figure 4.27	EDX measurement for coating on RABiT Ni produced from 0.30 mol/l Ce precursor solution and annealed at 1000°C for 1 h in reducing atmosphere. (a) Surface morphology measured, (b) table for element in at%.	100
Figure 4.28	FESEM image of the 45° tilt sample, produced using 0.30 mol/l Ce precursor solution on RABiT Ni and annealed at 1000°C for 1 h in Ar-5%H <sub>2</sub> .	100
Figure 4.29	XRD patterns of the coatings on RABiT Ni, produced using 0.30 mol/l solution and annealed at (a) 800°C, (b) 900°C, (c) 1000°C and (d) 1100°C respectively for 1 h in Ar-5%H <sub>2</sub> .	102
Figure 4.30	Raman shift for coating on RABiT Ni, deposited using 0.30 mol/l Ce precursor solution and annealed in Ar-5%H <sub>2</sub> at 1000°C for 1 h.	103
Figure 4.31	XRD patterns of coatings on RABiT Ni, produced from 0.30 mol/l Ce precursor solution and annealed at 1000°C for (a) 0.5 h, (b) 1 h, (c) 2 h, (d) 3 h and (e) 4 h in Ar-5%H <sub>2</sub> .	105
Figure 4.32	Plot of intensity ratio of (200) : (200)+(111) CeO <sub>2</sub> film on RABiT Ni, produced from 0.30 mol/l Ce precursor solution and annealed at 1000°C in Ar-5%H <sub>2</sub> for 0.5 h, 1 h, 2 h, 3 h and 4 h respectively.	106
Figure 4.33	Surface morphologies of film on RABiT Ni produced using 0.30 mol/l Ce precursor solution and annealed at 1000°C for (a) 0.5 h, (b) 2 h, (c) 3 h and (d) 4 h respectively in Ar-5%H <sub>2</sub> .	107

Figure 4.34	XRD patterns for coatings produced from 0.30 mol/l Ce precursor solution added with different volume % of methanol (annealed at 1000°C for 1 h in Ar-5%H <sub>2</sub> ).	110
Figure 4.35	Surface morphologies of film produced from 0.30 mol/l Ce precursor solution added with (a) 20 vol%, (b) 40 vol% and (c) 60 vol% methanol respectively (annealed at 1000°C for 1 h in Ar-5%H <sub>2</sub> ).	111
Figure 4.36	FESEM images of 45° tilt sample, produced using 0.30 mol/l Ce precursor solution added with (a) 20 vol%, (b) 40 vol% and (c) 60 vol% methanol respectively on RABiT Ni (annealed at 1000°C for 1 h in Ar-5%H <sub>2</sub> ).	112
Figure 4.37	Surface morphologies of film after being annealed at 1000°C for 1 h in Ar-5%H <sub>2</sub> , produced using 0.30 mol/l Ce precursor solution by using acetic acid as solvent.	113
Figure 4.38	FESEM images of 45° tilt sample, produced from 0.30 mol/l Ce precursor solution on RABiT Ni by using acetic acid as solvent (annealed at 1000°C for 1 h in Ar-5%H <sub>2</sub> ).	114
Figure 4.39	XRD patterns of the coatings produced from 0.30 mol/l Ce precursor solution by dissolving the cerium(III) acetate in (a) propionic acid and (b) acetic acid respectively (annealed at 1000°C for 1 h in Ar-5%H <sub>2</sub> ).	115
Figure 4.40	Characteristic of RABiT Cu substrate: (a) surface morphology viewed by FESEM, (b) surface roughness by AFM with RMS and R <sub>a</sub> values, and (c) XRD pattern.	116
Figure 4.41	Surface morphologies of coatings on RABiT Cu after being annealed at 1000°C for 1 h in Ar-5% H <sub>2</sub> produced from (a) 0.01 mol/l, (b) 0.03 mol/l, (c) 0.07 mol/l, (d) 0.10 mol/l, (e) 0.20 mol/l, (f) 0.30 mol/l and (g) 0.60 mol/l solution.	119
Figure 4.42	EDX measurement for coating on RABiT Cu after being annealed at 1000°C for 1 h in Ar-5% H <sub>2</sub> , produced from 0.01 mol/l solution. (a) SEM morphology, (b) table for element in at% for point A and B.	121
Figure 4.43	EDX measurement for coating on RABiT Cu after being annealed at 1000°C for 1 h in Ar-5% H <sub>2</sub> , produced from 0.30 mol/l solution. (a) Surface morphology measured, (b) table for element in at%.	121

Figure 4.44	EDX measurement for coating on RABiT Cu after being annealed at 1000°C for 1 h in Ar-5% H <sub>2</sub> , produced from 0.60 mol/l solution. (a) Surface morphology measured, (b) table for element in at%.	122
Figure 4.45	XRD patterns for coatings on RABiT Cu after annealed at 1000°C for 1 h in Ar-5%H <sub>2</sub> , produced from (a) 0.01 mol/l, (b) 0.03 mol/l, (c) 0.07 mol/l, (d) 0.10 mol/l, (e) 0.20 mol/l, (f) 0.30 mol/l and (g) 0.60 mol/l solution.	123
Figure 4.46	Raman shifts for as annealed samples produced from (a) 0.03 mol/l, (b) 0.30 mol/l and (c) 0.60 mol/l Ce precursor solution and etched with 0.10 mol/l HNO <sub>3</sub> for 1 s, 5 s and 10.	126
Figure 4.47	FESEM images for 45° tilt sample, produced using (a) 0.03 mol/l, (b) 0.30 mol/l and (c) 0.60 mol/l Ce precursor solutions respectively on RABiT Cu (annealed at 1000°C in Ar-5%H <sub>2</sub> for 1 h).	128
Figure 4.48	EDX measurement for 45° tilt sample of the coating after annealed at 1000°C for 1 h in Ar-5% H <sub>2</sub> , produced from 0.03 mol/l Ce precursor solution. (a) SEM morphology, (b) table for element in at% for point A and B.	129
Figure 4.49	EDX measurement for 45° tilt sample of the coating after annealed at 1000°C for 1 h in Ar-5% H <sub>2</sub> , produced from 0.30 mol/l Ce precursor solution. (a) SEM morphology, (b) table for element in at% for point A and B.	129
Figure 4.50	EDX measurement for 45° tilt sample of the coating after annealed at 1000°C for 1 h in Ar-5% H <sub>2</sub> , produced from 0.60 mol/l Ce precursor solution. (a) SEM morphology, (b) table for element in at% for point A and B.	130
Figure 4.51	XRD patterns for coatings on RABiT Cu, produced from (a) 0.03 mol/l, (b) 0.30 mol/l and (c) 0.60 mol/l Ce precursor solution and being etched for 10 s using 0.10 mol/l HNO <sub>3</sub> .	131
Figure 4.52	Surface morphologies of coatings produced using 0.30 mol/l Ce precursor solution and etched for 10 s using 0.10 mol/l HNO <sub>3</sub> (images on the left are the low magnification and on the right are the high magnification).	132



Figure 4.53	(a) 2D and (b) 3D images of AFM images with RMS and $R_a$ roughness values for the sample prepared using 0.30 mol/l Ce precursor solution and etched for 10 s.	132
Figure 4.54	The standard free energy change for the formation of selected metal oxides and buffer layer oxides, $\Delta G_T^0$ , between 300 K and 1300 K. The units of $\Delta G_T^0$ are $\text{kJ (mole O)}^{-1}$ .	133
Figure 4.55	Proposed mechanism for the formation of layered oxide structures on Cu in Ar-5% $\text{H}_2$ annealing atmosphere.	140
Figure 4.56	Schematic illustration of the layered oxide on RABiT Cu as a function of the concentration of the Ce precursor solution.	142
Figure 4.57	Surface morphologies of coatings on RABiT Cu after being annealed in Ar-5% $\text{H}_2$ for 1 h at (a) 800°C and (b) 900°C. All coatings were produced from 0.30 mol/l Ce precursor solution (dissolved in acetic acid and 20 vol% methanol).	144
Figure 4.58	2D images of AFM with their RMS and $R_a$ roughness values for coating on RABiT Cu after being annealed for 1 h in Ar-5% $\text{H}_2$ at (a) 800°C and (b) 900°C respectively, produced from 0.30 mol/l Ce precursor solution.	144
Figure 4.59	EDX measurement of coating annealed in Ar-5% $\text{H}_2$ for 1 h at (a) 800°C, produced from 0.30 mol/l Ce precursor solution. (a) Surface morphology measured, (b) table for element in at%.	145
Figure 4.60	EDX measurement of coating annealed in Ar-5% $\text{H}_2$ for 1 h at (a) 900°C, produced from 0.30 mol/l Ce precursor solution. (a) Surface morphology measured, (b) table for element at%.	145
Figure 4.61	FESEM images of 45° tilt samples, produced using 0.30 mol/l Ce precursor solutions on RABiT Cu and annealed at (a) 800°C and (b) 900°C for 1 h in Ar-5% $\text{H}_2$ .	146
Figure 4.62	EDX measurement for 45° tilt sample produced using 0.30 mol/l Ce precursor solution and annealed at 800°C for 1 h in Ar-5% $\text{H}_2$ . (a) SEM morphology, (b) table for element in at% for point A and B.	147

Figure 4.63	EDX measurement for 45° tilt sample produced using 0.30 mol/l Ce precursor solution and annealed at 900°C for 1 h in Ar-5% H <sub>2</sub> . (a) SEM morphology, (b) table for element in at% for point A and B.	147
Figure 4.64	Diffraction patterns of XRD for films annealed in Ar-5%H <sub>2</sub> for 1 h at (a) 800°C, (b) 900°C and (c) 1000°C, produced using 0.30 mol/l Ce precursor solution.	148
Figure 4.65	Raman shifts for films annealed in Ar-5%H <sub>2</sub> for 1 h at (a) 800°C, (b) 900°C, and (c) 1000°C respectively, produced from 0.30 mol/l Ce precursor solution.	149
Figure 4.66	Surface morphologies of coatings on RABiT Cu annealed at 1000°C for 1 h in vacuum, produced using (a) 0.01 mol/l, (b) 0.03 mol/l, (c) 0.07 mol/l, (d) 0.10 mol/l, (e) 0.20 mol/l, (f) 0.30 mol/l, (g) 0.40 mol/l and (h) 0.60 mol/l Ce precursor solutions.	152
Figure 4.67	EDX measurement of the coating on RABiT Cu after being annealed at 1000°C for 1 h in vacuum, produced using 0.30 mol/l Ce precursor solution. (a) Surface morphology measured, (b) table for element in at% for point A.	154
Figure 4.68	EDX measurement of the coating on RABiT Cu after being annealed at 1000°C for 1 h in vacuum, produced using 0.60 mol/l Ce precursor solution. (a) SEM morphology, (b) table for element in at% for point A and B.	155
Figure 4.69	(a) 2D and (b) 3D images of AFM of coating on RABiT Cu derived from 0.30 mol/l Ce precursor solution after being annealed at 1000°C for 1 h in vacuum.	155
Figure 4.70	FESEM images of the 45° tilt samples, produced using (a) 0.03 mol/l and (b) 0.30 mol/l Ce precursor solution on RABiT Cu after being annealed at 1000°C for 1 h in vacuum.	157
Figure 4.71	XRD patterns for coatings on RABiT Cu after being annealed at 1000°C for 1 h in vacuum, produced using different concentrations of Ce precursor solution as stated.	160
Figure 4.72	Raman shifts for coatings on RABiT Cu after being annealed at 1000°C for 1 h in vacuum produced using different Ce precursor solution concentrations as stated.	161

Figure 4.73	XRD pattern for the sample after being etched for 5 s. The sample was produced using 0.30 mol/l Ce precursor solution and annealed at 1000°C for 1 h in vacuum.	162
Figure 4.74	Raman shifts for the sample after being etched for 1 s, 5 s and 10 s respectively. The sample was produced using 0.30 mol/l Ce precursor solution and annealed at 1000°C for 1 h in vacuum.	162
Figure 4.75	Surface morphologies for samples produced using 0.30 mol/l Ce precursor solution and etched with 0.10 mol/l HNO <sub>3</sub> for 5 s.	163
Figure 4.76	2D and 3D AFM images for samples produced using 0.30 mol/l Ce precursor solution and etched with 0.10 mol/l HNO <sub>3</sub> for 5 s.	163
Figure 4.77	Surface morphologies of coating on RABiT Cu after being annealed in vacuum for 1 h at (a) 700°C, (b) 800°C, (c) 900°C and (d) 1000°C, produced using 0.30 mol/l Ce precursor solution.	164
Figure 4.78	XRD patterns for coating on RABiT Cu after being annealed in vacuum for 1 h at different temperatures, produced using 0.30 mol/l Ce precursor solution.	165
Figure 4.79	FESEM images of bended and 45° tilt samples, produced using 0.30 mol/l Ce precursor solution on RABiT Cu and annealed at (a) 800°C and 900°C for 1 h in vacuum (images on the left are the low magnification and on the right are the high magnification).	166
Figure 4.80	Raman shifts for coatings on RABiT Cu after being annealed in vacuum for 1 h at different temperatures, produced using 0.30 mol/l Ce precursor solution.	167
Figure 4.81	Surface morphologies of coating on RABiT Cu after being annealed at 1000°C in vacuum for (a) 10 min, (b) 30 min, (c) 2 h, and (d) 3 h respectively, produced using 0.30 mol/l Ce precursor solution.	169
Figure 4.82	XRD patterns for coating on RABiT Cu after being annealed at 1000°C in vacuum for different times, produced using 0.30 mol/l Ce precursor solution.	170

Figure 4.83	Raman shifts for coating on RABiT Cu after being annealed at 1000°C in vacuum for different times, produced using 0.30 mol/l Ce precursor solution.	171
Figure 4.84	Proposed mechanism of the oxides formation on RABiT Cu in vacuum annealing atmosphere.	172

## LIST OF ABBREVIATIONS

1G	First generation
2G	Second generation
AC	Alternating current
AFM	Atomic force microscopy
Ag	Silver
$B_c$	Critical magnetic field
Ce	Cerium
$Ce_2O_3$	Cerium (III) oxide
$CeO_2$	Ceria
Cr	Chromium
CSD	Chemical solution deposition
Cu	Copper
CuO	Copper(II) oxide
$Cu_2O$	Copper(I) oxide
CVD	Chemical vapour deposition
EDX	Energy dispersive X-ray
FCC	Face centred cubic
Fe	Iron
FESEM	Field emission scanning electron microscopy
Hg	Mercury
HTS	High temperature superconductor
I	Intensity
IBAD	Ion-Beam-Assisted Deposition
ICDD	International centre for diffraction data

ISD	Inclined-Substrate Deposition
$J_c$	Critical current density
$J_{ENG}$	Engineering current density
LBCO	Lanthanum barium copper oxide
LAO	Lanthanum aluminum oxide
LPE	Liquid phase epitaxy
LZO	Lanthanum zirconate
MBE	Molecular beam epitaxy
$MgB_2$	Magnesium diboride
Ni	Nickel
PLD	Pulsed laser deposition
p	Partial pressure
R	Resistivity
$R_a$	Average surface
RABiT	Rolling-Assisted-Biaxially-Textured
RE	Rare-earth
RMS	Root-mean-square
$T_c$	Critical temperature
TFA	Trifluoroacetate
TG	Thermogravimetric
V	Vanadium
XRD	X-ray diffraction
$Y_2O_3$	Yttrium Oxide
YBCO	Yttrium barium copper oxide
YSZ	Yttria stabilised zirconia

## LIST OF SYMBOLS

$\text{\AA}$	Angstrom
$\theta$	Diffraction angle ( $^{\circ}$ )
$\lambda$	Wavelength ( $\text{\AA}$ )
D	Crystallite size (nm)
B	Line broadening of full width at half maximum (radian)
$\Delta G_T$	Gibbs free energy change at a temperature ( $\text{J}\cdot\text{mol}^{-1}$ )
$\Delta G^*$	Thermodynamic energy barrier ( $\text{J}\cdot\text{mol}^{-1}$ )
$\Delta G_v$	Free energy difference per volume ( $\text{J}\cdot\text{m}^{-3}$ )
$\square$	Surface energy (J)

**PEMBENTUKAN LAPISAN PENIMBAL SERIUM OKSIDA UNTUK  
SUPERKONDUKTOR  $\text{YBa}_2\text{Cu}_3\text{O}_{7-x}$**

**ABSTRAK**

Filem  $\text{CeO}_2$  telah dibentuk di atas substrat Cu dan Ni bertekstur yang dibantu penggelekan (RABiT) melalui kaedah penguapan larutan kimia (CSD) secara penguraian logam organik. Filem  $\text{CeO}_2$  akan digunakan sebagai lapisan penimbal untuk aplikasi konduktor bersalut YBCO. Parameter eksperimen yang dikaji adalah kepekatan larutan prapenanda Ce, jenis pelarut yang digunakan, peratusan isipadu methanol dan keadaan penyepuhlindapan: suhu, masa dan atmosfera. Larutan prapenanda yang digunakan ialah serium(III) asetat dilarutkan di dalam asid propionik atau asid asetik dan methanol. Larutan prapenanda diputarkan di atas substrat pada kelajuan 4000 rpm dan diikuti dengan penyepuhlindapan. Filem  $\text{CeO}_2$  yang seragam, bebas daripada keretakan dan mempunyai epitaksi dihasilkan daripada larutan prapenanda Ce 0.30 mol/l yang ditambah 20 % isipadu methanol dan disepuhlindap di dalam  $\text{Ar-5\%H}_2$  selama sejam pada  $1000^\circ\text{C}$ . Tiada lapisan perantaraan terhasil di antara filem  $\text{CeO}_2$  dengan substrat Ni. Ketebalan filem ialah dianggarkan 25 nm dan kelekatan filem di atas substrat adalah baik. Kekasaran filem secara umumnya ialah 7 nm. Sebaliknya, di atas Cu RABiT, tindak balas yang hebat boleh dilihat diantara lapisan  $\text{CeO}_2$  dan substrat. Sampel-sampel yang disepuhlindap dalam  $\text{Ar-5\%H}_2$  selama sejam pada  $1000^\circ\text{C}$  terdiri daripada  $\text{CeO}_2$  (lapisan permukaan) |  $\text{Cu}_2\text{O}$  (nodular) |  $\text{Cu}_2\text{O}$  (lapisan padat) di atas Cu. Filem (200)  $\text{Cu}_2\text{O}$  dikesan apabila lapisan permukaan dan lapisan bernodul dipunar. Sampel yang disepuhlindap di dalam vakum selama sejam pada  $1000^\circ\text{C}$  terdiri daripada  $\text{CeO}_2$



(lapisan permukaan) |  $\text{CeO}_2$  yang diturunkan (padat) | atas Cu. Pembentukan lapisan oksida atas Cu dalam Ar-5% $\text{H}_2$  dan vakum telah dicadangkan.

# FORMATION OF CERIA BUFFER LAYER FOR $\text{YBa}_2\text{Cu}_3\text{O}_{7-x}$ SUPERCONDUCTORS

## ABSTRACT

$\text{CeO}_2$  films were formed on rolling-assisted-biaxially-textured (RABiT) Ni and Cu substrates by chemical solution deposition (CSD) method via metal organic decomposition (MOD) route. The  $\text{CeO}_2$  film is to be used as a buffer layer for YBCO coated conductor application. Experimental parameters that were carried out were the concentration of Ce precursor solution, type of solvent used, volume percent of methanol and annealing treatment process: the temperature, time and atmosphere. The precursor solution used was cerium(III) acetate dissolved in either propionic acid or acetic acid and added with methanol. The precursor solution was spin coated on the substrate at the speed of 4000 rpm and followed by annealing. The homogeneous, crack free and epitaxial  $\text{CeO}_2$  film was produced on RABiT Ni by using 0.30 mol/l Ce precursor solution added with 20 vol% methanol and annealed in Ar-5% $\text{H}_2$  for an hour at 1000°C. No interfacial layer between the  $\text{CeO}_2$  layer and Ni substrate was observed. The thickness of the film was estimated to be 25 nm and the adherency of the film on the substrate was good. Typical roughness, in RMS of the film was 7 nm. On the other hand, on RABiT Cu, severe interfacial reaction was seen. Samples annealed in Ar-5% $\text{H}_2$  for an hour at 1000°C are consisted of  $\text{CeO}_2$  (surface layer) |  $\text{Cu}_2\text{O}$  (nodules) |  $\text{Cu}_2\text{O}$  (compact) on Cu. When the surface layer and the porous nodules were etched, a flat (200)  $\text{Cu}_2\text{O}$  film was seen. Samples annealed in vacuum for an hour at 1000 °C are consisted of  $\text{CeO}_2$  (surface layer) | reduced  $\text{CeO}_2$  (compact)

on Cu. The formation of the layered oxides on Cu in Ar-5% $H_2$  and vacuum were proposed.

# CHAPTER 1

## INTRODUCTION

### 1.1 Introduction

Since the discovery of cuprate based high temperature superconductors (HTSs), great efforts have been focused on the development of high current carrying capability superconductor wire. Yttrium barium copper oxide,  $\text{YBa}_2\text{Cu}_3\text{O}_{7-x}$  (YBCO) is the most promising cuprate HTS material as its critical temperature ( $T_c$ ) is above the boiling point of liquid nitrogen and the critical current density ( $J_c$ ) is in the range of  $10^4 \text{ Acm}^{-2}$  to  $10^6 \text{ Acm}^{-2}$ . Nonetheless, to achieve high  $J_c$ , the YBCO must have perfect crystal alignment. The use of YBCO single crystal can be done but this would translate to extremely high cost.

Therefore YBCO must be grown with perfect grain orientation on a textured substrate. YBCO grains must all be at (100) orientation and  $\langle 001 \rangle$  growth direction. Thin YBCO layer is deposited epitaxially on textured template giving rise to a so called coated conductor tape. YBCO coated conductor is generally consisted of YBCO superconducting layer on a buffered metallic substrate.

The buffer layer isolates YBCO from the metallic substrate of Ni and Cu as well as to transfer the texture from substrate to YBCO. Isolation of Ni from YBCO is vital as Ni reacts with YBCO. One major impediment on the commercialization of YBCO coated conductor is on the cost of producing the wire. In this project,  $\text{CeO}_2$  film is studied as buffer layer which serves as a template for the epitaxial growth of

YBCO layer.  $\text{CeO}_2$  is chosen because it has compatible thermal coefficient, crystalline lattice parameter match and chemical stability with the YBCO. As a good buffer layer for YBCO coated conductor,  $\text{CeO}_2$  buffer layer must be smooth, crack free and has preferred orientation, i.e., (100)  $\langle 001 \rangle$  cube texture on the substrate. The use of chemical process for buffer layer deposition is seen as interesting and efficient way to contribute in lowering the cost of the coated conductor.

### **1.1 Objectives**

The first objective of this research project is to produce  $\text{CeO}_2$  thin film on rolling-assisted-biaxially-textured (RABiT) Ni by chemical solution deposition (CSD). The  $\text{CeO}_2$  film produced is to be used as a buffer layer for YBCO coated conductor application and hence it has to be smooth, crack free and textured. Besides, low cost and simple process is required for the deposition of  $\text{CeO}_2$  buffer layer.

The second objective is to assess the formation of  $\text{CeO}_2$  layer on RABiT Cu. Cu substrate was studied as an alternative substrate to ferromagnetic Ni substrate for coated conductor application due to its excellent properties such as diamagnetism, low resistivity, high thermal conductivity and easily developed cube textured.

### **1.3 Research Motivation**

For achieving high critical current density in YBCO coated conductor, elimination of weak links between YBCO grains is one of the crucial requirement. Weak links are produced by large angle grain boundaries of YBCO caused by the misalignment of the grains. Therefore the key is to prepare a textured buffer layer on a textured metallic substrate which transmit the underneath texture to the YBCO

layer. RABiT based substrate is a commonly used template for the epitaxial growth of buffer layer. CSD is emerged as a low cost process to deposit a biaxially textured buffer layer on the RABiT based substrate. However texturing and cracking of buffer layer is the common problems in the non-vacuum methods. So the precursor solution used for the formation of buffer layer must be chosen properly and optimised. In here, epitaxial growth of  $\text{CeO}_2$  film on Ni-based substrate, produced from cerium(III) acetate dissolved in carboxylic acid, i.e., propionic acid and acetic acid had been investigated. To date, not many works have been reported on the use of this precursor solution.

Furthermore, the ferromagnetic property of Ni substrate causes a significant reduction of critical current density in the power application. Cu substrate is seen as a potential substrate candidate to replace Ni substrate for the YBCO coated conductor development. However to date there is no reported work on the formation of  $\text{CeO}_2$  on Cu substrate by CSD. In here, formation of  $\text{CeO}_2$  film on RABiT Cu substrate had been investigated.

#### **1.4 Scope of Investigation**

In this project, deposition of  $\text{CeO}_2$  film on metallic substrates by CSD using cerium(III) acetate as starting Ce salt was investigated. Three different substrates were used as the template for the deposition of  $\text{CeO}_2$ , i.e., polycrystalline Ni, RABiT Ni and RABiT Cu. Growth mechanism was proposed in order to understand the behaviour of  $\text{CeO}_2$  with different deposition conditions.

Parameters studied for the formation of CeO<sub>2</sub> film on polycrystalline Ni substrate include concentration of Ce precursor solution and annealing temperature. The problem of polycrystalline Ni substrate is the formation of randomly orientated CeO<sub>2</sub> film. Further investigation of epitaxial growth of CeO<sub>2</sub> film was performed on RABiT Ni substrate. Effect of annealing temperature, annealing time, volume percent of methanol and type of solvent to the formation of CeO<sub>2</sub> film were investigated.

After obtaining (200) CeO<sub>2</sub> film with good reproducibility, the focus of the research was shifted to the formation of CeO<sub>2</sub> film on RABiT Cu. The problem of the epitaxial growth of CeO<sub>2</sub> on RABiT Cu is the oxidation of Cu. Several parameters were studied including concentration of Ce precursor solution, annealing temperature, annealing time and annealing atmosphere.

## **1.5 Outline of Chapter**

This thesis is divided into five chapters. Chapter 1 consists of introduction, objective, research motivation and scope of investigation in this project. For chapter 2, the introduction of superconductivity and YBCO superconducting coated conductor is presented. Besides, literature review related to the development of textured buffer layer for YBCO coated conductor application such as substrates, buffer layers and deposition techniques are discussed. Chapter 3 covers the experimental procedure, different parameters studied and characterizations techniques involved throughout the research. In chapter 4, discussions of all the results obtained in this project as well as the growth mechanism of CeO<sub>2</sub> formation

are presented. Finally, conclusion and achievement of this project are summarised in chapter 5, together with some suggestion for future work.



## CHAPTER 2

### LITERATURE REVIEW

#### 2.1 Introduction

In this chapter, a brief introduction of the phenomenon of superconductivity followed by a description on coated conductor based on YBCO is presented. A review on the major issues governing the role of the buffer layer and substrate in coated conductor development and the latest progress made in order to curb the limitation of the existing buffered substrate is presented. Oxide buffer layers commonly used and recently developed are reviewed especially on the characteristic of the materials and deposition techniques. As  $\text{CeO}_2$  is the oxide of choice in this thesis, it is reviewed in great depth particularly on the chemical solution deposition (CSD) process for the formation of the  $\text{CeO}_2$  thin film. At the end of this chapter, the current status of the coated conductor development in term of YBCO deposition has been briefly discussed.

#### 2.2 Introduction of Superconductivity

Superconductivity was first discovered in 1911 when mercury (Hg) was cooled down below 4.2 K by Heiki Kamerlingh Onnes (Vendik *et al.*, 2000). As shown in Figure 2.1, superconductivity is a phenomenon in which a material losses all its electrical resistance upon cooling below a critical transition temperature ( $T_c$ ). Above  $T_c$ , the material is in its normal state and does have resistance hence the flow of electric current is accompanied by the production of heat and the dissipation of energy (Vemulakonda *et al.*, 2007, Smart and Moore, 2005). For a typical metal,

resistivity reduces at low temperature but would never reach zero as shown in Figure 2.1. This is to follow Matthiessen's rule.

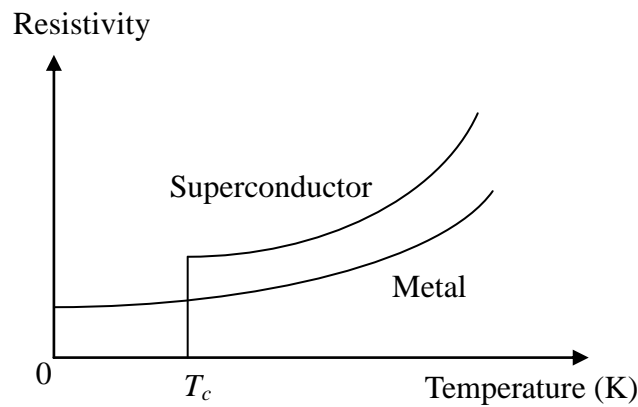


Figure 2.1: Temperature dependence of electrical resistivity of a superconductor (Callister, 2003).

For a material to be considered as a superconductor, it has to exhibit two distinctive properties: (1) zero resistivity ( $R=0$  at  $T < T_c$ ) and (2) Meissner effect. When a superconductor is cooled below its  $T_c$ , the cloud of individual electrons that characterizes the normal state transforms themselves into quantum fluid of highly correlated pairs of electrons. A conduction electron of a given momentum and spin gets weakly coupled with another electron of exactly the opposite momentum and spin. These pairs are called 'Cooper Pairs' and they all move in a single coherent motion. Once this collective, highly coordinated, state of coherent 'Cooper pairs' is set into motion, the movement is resistanceless. No scattering of the coherent fluid would occur and creating zero resistivity conductivity (Callister, 2003).

Meissner effect is a phenomenon where no magnetic induction inside the superconductor when the material is cooled below  $T_c$  in the presence of external magnetic field below the critical magnetic field ( $B_c$ ). This occurs because magnetic

flux is expelled from the interior of the material as shown in Figure 2.2. Nonetheless, there is a type of superconductor which allows the penetration of the magnetic field inside its body. This will be considered in the sub heading 2.3.

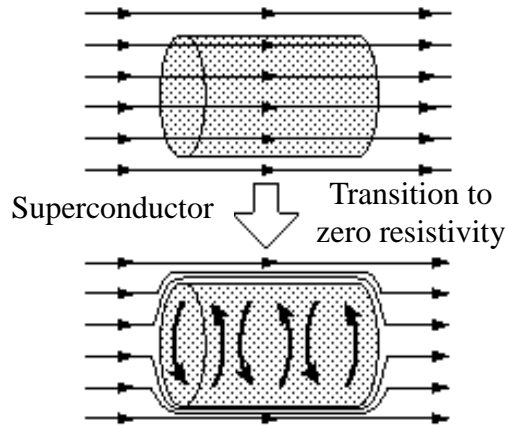


Figure 2.2: Meissner effect for Type I superconductor.

The current that flows in a superconductor at a certain temperature and a fixed magnetic field is called critical current density ( $J_c$ ).  $J_c$  is defined as the critical current of a superconductor divided by the cross sectional area of the superconductor material. It is the maximum current that a superconductor can carry at a particular field.  $J_c$  is useful when characterizing the quality of a superconductor. Another term worth defining is engineering current density ( $J_{ENG}$ ).  $J_{ENG}$  is the critical current of the wire divided by the cross sectional area of the entire wire, including both superconductor and normal metal materials. The  $J_{ENG}$  is an important parameter used in the design of applications based on HTS wires (Kim *et al.*, 2006).

### 2.3 Type I and Type II Superconductors

Generally, superconductors are classified into Type I and Type II based on their  $T_c$  and magnetic properties. Figure 2.3 (a) and (b) show the behaviour of Type I and Type II superconductors respectively as a function of applied magnetic field.

Type I superconductors behave as perfect diamagnetic materials. They require extremely low temperatures for them to be superconducting as well as to repel the magnetic field until their  $B_c$  is reached. Above  $B_c$ , the materials go back to the normal state as shown in Figure 2.3 (a). The type I superconductors have been of limited practical usefulness because of the low  $T_c$  and  $B_c$ .

Type II superconductors have much higher  $T_c$  and  $B_c$  compared to Type I superconductors upon the application of magnetic field. Type II superconductors behave as Type I superconductors until the magnetic field reaches a lower  $B_{c1}$  value. Above this field, a mixed state or a 'vortex state' is achieved. The magnetic started to penetrate in the materials in a form of vortex until reaching an upper  $B_{c2}$  as shown in Figure 2.3 (b). Each of the vortices carries significant current. Vortices can be viewed as cylindrical tubes of magnetic flux with high supercurrent circulating at the surface of each cylinder. Due to the circulating current around each vortex, a type II superconductor can carry much higher  $J_c$ . Examples of Type I and Type II low temperature superconductors with their  $T_c$  values are listed in Table 2.1. In this table only the metallic and intermetallic compounds are listed. Ceramic oxide superconductor will be discussed in the sub-topic 2.4. To date, Nb based compounds are the most used and commercialize superconducting materials.

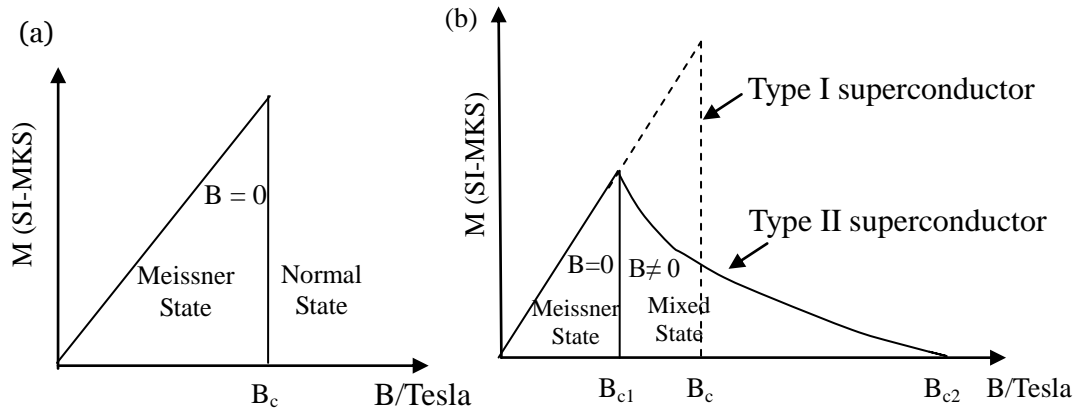


Figure 2.3: Magnetization ( $M$ ) as the function of applied magnetic field for (a) Type I and (b) Type II superconductors (Cyrot and Pavuna, 1992).

Table 2.1: Example of Type I and Type II low temperature superconductors and their  $T_c$  values.

Low temperature superconductors	Type	$T_c$ (K)
Hg	I	4.1
Sn	I	3.7
In	I	3.4
Al	I	1.9
Zn	I	0.9
Zr	I	0.6
La	I	4.9
Mo	I	0.9
Ti	I	0.4
Cd	I	0.5
ZrB <sub>12</sub>	I	6.0
Nb <sub>3</sub> Sn	II	18.3
NbTi	II	10
NbN	II	16
Nb <sub>3</sub> Al	II	18
Nb <sub>3</sub> Ge	II	23.2
NbO	II	1.4
YB <sub>6</sub>	II	8.4
Ba <sub>8</sub> Si <sub>46</sub>	II	8.1
C <sub>60</sub> K <sub>3</sub>	II	19.8

Generalizing superconductor by its magnetic and electrical behavior is acceptable. However, in 2001, a so-called intermediate temperature MgB<sub>2</sub> superconductor was discovered by Akimitsu *et al.* MgB<sub>2</sub> has a T<sub>c</sub> of 39 K and J<sub>c</sub> of 10<sup>5</sup> Acm<sup>-2</sup>. The discovery of MgB<sub>2</sub> has offered a new class of simple and low cost binary intermetallic superconductor (Mijatovic *et al.*, 2002, Kumakura *et al.*, 2002). Substantial research attention has been paid to MgB<sub>2</sub> with the hope of finding some applications at liquid hydrogen temperature (20 K) (Glowacki *et al.*, 2003). However the growth of MgB<sub>2</sub> is complicated due to the large difference in vapour pressure between Mg and B and the high sensitivity of magnesium to oxidation. To overcome these two complicated factors, very low oxygen partial pressures in the deposition system must be used.

In 2008, a pnictide compound was reported to be superconducting as well. Superconducting pnictide compounds are consisted of layered FeAs compounds with T<sub>c</sub> of 26 K. The parent compound, LaOFeAs-1111 was not superconducting, but upon replacing some of the oxygen by fluorine (LaFeAs(O<sub>1-x</sub>F<sub>x</sub>)), the material became superconducting (Norman, 2008). The pnictide compound is an anti-ferromagnet at low doping and increased doping destroys the anti-ferromagnetism leading to superconductivity. Apart from doping, high pressure is also reported to be one of the possible ways to increase the T<sub>c</sub> from 26 K to about 50 K (Chu *et al.*, 2009). In general, superconducting Fe-pnictides are grouped into four homologous series, 1111 (ROFeAs with R = rare-earth, AeFeAs with Ae = alkaline earth), 122 (AeFeAs, AFeAs with A = alkaline), 111 (AFeAs) and 011 (FeSe). When Fe-pnictide compounds were properly doped, the maximum T<sub>c</sub> values achieved are about 55 K, 38 K, 12-25 K and 9-14 K for 1111, 122, 111 and 011 respectively. One

major drawback on the use of this compound is its toxicity as it contains As and F. Nonetheless, many research works are being carried out on this type of superconductor.

## 2.4 Cuprate High Temperature Superconductors

High temperature superconductor (HTS) is resistance-free conductors made of ceramic materials with  $T_c > 30$  K. Cuprate HTS adopt a perovskite structure. Lanthanum barium copper oxide,  $\text{La}_{2-x}\text{Ba}_x\text{CuO}_4$  with the  $T_c$  of 35 K was the first HTS discovered in 1986 by Bednorz and Muller. The discovery was soon followed by yttrium barium copper oxide,  $\text{YBa}_2\text{Cu}_3\text{O}_{7-x}$  (often called Y-123 or YBCO) with the  $T_c$  of 92 K in 1987 (Togano, 2003). This moved the  $T_c$  of superconducting materials from the range of liquid helium temperature (4.2 K) to those of liquid nitrogen temperature (77 K). The significance of the discovery of HTS with the  $T_c$  above boiling point of liquid nitrogen is the reduction of cost for superconductor refrigeration (Jones, 2008). Table 2.2 lists examples for cuprate HTS with their  $T_c$  and  $J_c$  value at zero field.

Table 2.2: Example of cuprate HTS with their  $T_c$  and  $J_c$  at zero field (Zhao *et al.*, 1995, Togano, 2003, Kumar *et al.*, 2005, Hu *et al.*, 1997, Hu *et al.*, 1996, Liou *et al.*, 1991, Meng *et al.*, 1998).

Cuprate HTS	Notation	$T_c$ (K)	$J_c$ (0 H)
$\text{La}_{1.85}\text{Sr}_{0.15}\text{CuO}_4$	LSCO	35	-
$\text{Nd}_{1.85}\text{Ce}_{0.15}\text{CuO}_4$	NCCO	23	-
$\text{YBa}_2\text{Cu}_3\text{O}_7$	YBCO	92	$10^6$ A/cm <sup>2</sup>
$(\text{Bi,Pb})_2\text{Sr}_2\text{Ca}_2\text{Cu}_3\text{O}_x$	$(\text{Bi,Pb})_2\text{SCCO}$	110	-
$\text{Bi}_2\text{Sr}_2\text{CaCu}_2\text{O}_8$	Bi-2212	80	$10^3$ A/cm <sup>2</sup>
$\text{Bi}_2\text{Sr}_2\text{Ca}_2\text{Cu}_3\text{O}_{10}$	Bi-2223	108	$10^3$ A/cm <sup>2</sup>
$\text{Ti}_2\text{Ba}_2\text{CuO}_6$	Ti-2201	80	$10^6$ A/cm <sup>2</sup>
$\text{Ti}_2\text{Ba}_2\text{CaCu}_2\text{O}_8$	Ti-2212	100	$10^6$ A/cm <sup>2</sup>
$\text{Ti}_2\text{Ba}_2\text{Ca}_2\text{Cu}_3\text{O}_{10}$	Ti-2223	120	$10^6$ A/cm <sup>2</sup>

Table 2.2: Example of cuprate HTS with their  $T_c$  and  $J_c$  at zero field (Zhao *et al.*, 1995, Togano, 2003, Kumar *et al.*, 2005, Hu *et al.* , 1997, Hu *et al.*, 1996, Liou *et al.*, 1991, Meng *et al.*, 1998) (*cont.*).

Cuprate HTS	Notation	$T_c$ (K)	$J_c$ (0 H)
HgBa <sub>2</sub> CuO <sub>4</sub>	Hg-1201	94	-
HgBa <sub>2</sub> CaCu <sub>2</sub> O <sub>6</sub>	Hg-1212	121	10 <sup>6</sup> A/cm <sup>2</sup>
HgBa <sub>2</sub> Ca <sub>2</sub> Cu <sub>3</sub> O <sub>10</sub>	Hg-1223	134	10 <sup>4</sup> A/cm <sup>2</sup>
Pb <sub>2</sub> Sr <sub>2</sub> Y <sub>0.5</sub> Ca <sub>0.5</sub> Cu <sub>3</sub> O <sub>x</sub>	(Pb,Sr) <sub>2</sub> YCCO	70-80	-

Among these HTS compounds, YBCO is the most promising material to be used as HTS wire for power transmission cable application. Ti and Hg-based HTS compounds are toxic and hence dangerous and are not environmentally friendly. On the other hand, Bi-based HTS tapes have large electronic anisotropy and associated weak flux pinning problem which limit the use for low magnetic field applications. YBCO on the other hand includes neither toxic elements nor volatile compounds. YBCO also have less anisotropic than other HTS materials and is able to carry higher  $J_c$  at higher magnetic fields.

HTS wire based on YBCO is known as second generation (2G) superconducting wire. It is consisted of epitaxial YBCO film deposited on a textured buffered metallic substrate and is called YBCO coated conductor as shown in Figure 2.4 (Knoth *et al.*, 2006). By preparing a good surface texture of buffered metallic substrate, YBCO with low angle grain boundaries can be grown on top of it and high current can flow through the a-b planes direction easily as shown in Figure 2.5 (a). Figure 2.5 (b) shows the crystal structure of YBCO which is described as an oxygen-depleted layered perovskite structure, formed as Cu-O layer sandwiched between layers containing other elements in the compound.



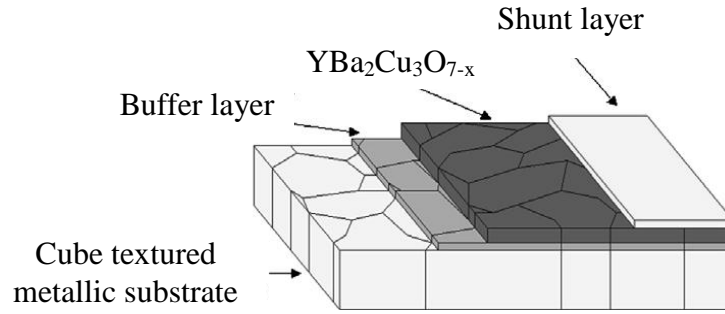


Figure 2.4: Typical architecture of YBCO coated conductor (Knoth *et al.*, 2006).

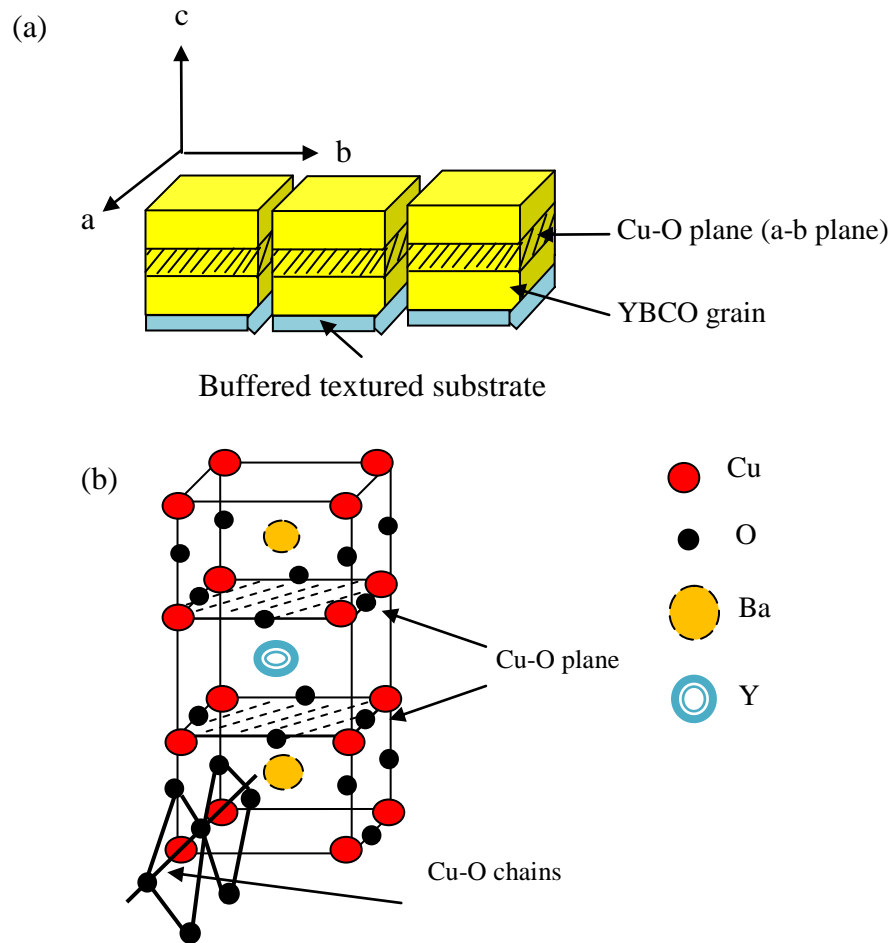


Figure 2.5: (a) YBCO grains grown on buffered textured substrate with low angle grain boundaries, (b) crystal structure of YBCO.

Superconducting wires which are based on  $\text{Bi}_2\text{Sr}_2\text{Ca}_2\text{Cu}_3\text{O}_{10}$  (Bi-2223) are called first generation (1G) HTS wire. This wire is made ‘Oxide Powder in Tube’ (OPIT) method where Bi-2223 are put in an Ag and then drawn to form powder in

tube wires. Uniaxial crystal is obtained by the means of thermo-mechanical deformation (Driessche *et al.*, 2005). High strength and flexible, kilometer length 1G HTS wire has been now commercialized. However this 1G HTS wire has low current carrying capability in high magnetic field at 77 K as well as undesired intrinsic properties.

Instead, the YBCO possesses some advantages compared to Bi-2223 and was found to be an alternative material for the production of HTS wire. The main advantages of YBCO are:

- (a) YBCO has high current carrying capability and it is able to achieve high  $J_c$  in the MA/cm<sup>2</sup> range at 77 K.
- (b) The AC losses in YBCO tape are lower than in a Bi-2223 tape due to greatly thinner YBCO layer.
- (c) The production cost of YBCO tape is cheaper than Bi-2223 tape because YBCO tape uses less costly components (such as silver) than a Bi-2223 tape.

Besides inducing the texture to YBCO by using textured buffered substrate, introduction of flux pinning centres on the buffered substrate can also help to enhance the  $J_c$  of YBCO coated conductor [Solovyov *et al.*, 2010]. Flux pinning centres can be introduced by engineering the surface of the buffer layer so that it consists of dispersed oxide with nanosized features for example nanoislands. Dispersion of nanoislands on a buffer layer can introduce ordered crystalline defects in YBCO. Due to the mismatch between pinning centres and YBCO film, some strain would be exerted into the YBCO film. The strain field are

expected to provide additional flux pinning defects in the YBCO film, thus enhances the  $J_c$  performance in the presence of high magnetic field (Cui *et al.*, 2007).

Due to the fact that buffered textured metallic substrate plays an important role in producing a high performance YBCO coated conductor, substrate and oxide buffer layer for YBCO development are to be discussed here.

## **2.5 Substrate**

Substrate is often seen as a passive part of the whole coated conductor configuration, and hence there is a strong tendency to ignore and to assume that its role is solely as a template of growth. Nonetheless, the substrate is one of the most important parts of the coated conductor and selecting suitable substrate has remained a challenge. Therefore, the quest for suitable substrate materials that are capable of supporting epitaxial YBCO film has been an active research topic.

### **2.5.1 Substrates Requirements for YBCO Coated Conductor**

To form cube textured YBCO film, the characteristic of the substrate without doubt plays an important role. The following summarises some of these characteristics.

Surface quality: A uniform, smooth and clean surface of substrate is necessary since it is here that the film and substrate interaction occurs. Uniformity, smoothness and cleanliness of substrate have a significant impact on film nucleation, morphology and structure. Apart from that, the substrate must also provide a highly textured surface to reduce defects on the YBCO film.

Chemical inertness: There should not be any chemical reactions between the substrate and YBCO. This is because the chemical reaction between substrate and YBCO would dampen superconductivity in YBCO. This constraint is especially severe if the deposition of film is via chemical methods. The precursor solution with high reactivity might react with substrate and form interfacial layer. The interfacial layer would hinder the epitaxial growth of the YBCO. Furthermore, YBCO is a reactive compound, substrate like Si is an attractive choice but YBCO reacts with Si.

Lattice matching: Substrate should have lattice parameter that compatible with the YBCO film. Large lattice mismatch between substrate and YBCO film would insert a stress or strain to the film that exerts a decisive influence on epitaxial growth of film (Khodan *et al.*, 2000, Engel *et al.*, 2005).

Thermal properties: Substrate and YBCO film must have less mismatch in coefficient of thermal expansion. Large coefficient of thermal expansion between the substrate and YBCO may result in loss of adhesion, film cracking or film buckling during thermal cycling. Besides, the substrate has to be thermodynamically stable at the processing temperature range to prevent the oxidation of substrate and phase transition.

Mechanical properties: It has to be mechanically robust as means to protect the brittle YBCO. The tensile strength of the substrate must not change within the temperature range required to grow and process the thin film.

Single crystal ceramic substrate was used as textured template for YBCO growth due to the excellent crystallographic texture, often related to the feature of its surface, smooth and uniform and is nonreactive. Nonetheless in late 1990s, metallic substrates are seen to be more functional and attractive due to its mechanical robustness and flexibility. For the application of flexible coated conductor, metallic substrate could give a mechanical protection to the brittle YBCO film. Besides, long length coated conductor can be produced due to the increases of flexibility. Furthermore it can be used as an alternative current carrying path and also acts as heat sink, in the event of electrical breakdown in the YBCO film. However, before the metallic substrate can be used, the surface quality in term of its texture must first be optimised.

There are currently three common processes for obtaining biaxially textured metallic substrates for YBCO coated conductor. The first approach is rolling-assisted-biaxially-textured-substrate (RABiTS) process which was invented by Oak Ridge National Lab (ORNL) (Goyal *et al.*, 1999, Sheth *et al.*, 1998). The second one is ion-beam-assisted deposition (IBAD) process invented by Iijima *et al.* (Wang *et al.*, 2009). The other method is the inclined substrate deposition (ISD) process (Sheth *et al.*, 1998). The following sub heading 2.5.2 explains each of the method.

### **2.5.2 Rolling-Assisted-Biaxially-Textured-Substrates (RABITS) Process**

In RABiTS process, the starting un-textured metal foil (often in a form of a strip) is cold rolled and then annealed to promote a particular textured surface as shown in Figure 2.6. After the metal is textured, a thin layer of a buffering material will be coated on the metallic foil. The buffer layer produced is important since it

helps to transfer the alignment from the metal surface to the superconductor layer while avoiding chemical degradation of the superconductor. Finally, epitaxial growth of superconductor layer is deposited onto the buffer layers.

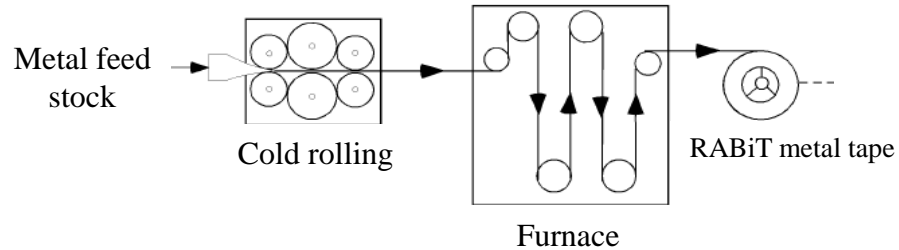


Figure 2.6: Schematic illustration of textured substrate preparation method using RABiTS process (Sheth *et al.*, 1998).

### 2.5.2.1 RABiT Substrate

The basic requirement for the formation of textured metallic substrate via RABiTS process is that it can generate desired texture by rolling and recrystallization process. Metals of interest include cubic metals and its alloys such as face-centered cubic (FCC) Ni and its alloys. FCC materials can be developed into extremely sharp cube texture of orientation  $(100) \langle 001 \rangle$  after recrystallization.

Ag is the first candidate material that has been used as a template for the subsequent growth of superconducting layer. This is because Ag is benign to YBCO and has a good compatibility with YBCO (Phillips, 1996). However, it is very difficult to achieve the monovariant brass texture or cube texture in Ag. Large value of lattice misfit and thermal expansion coefficient between Ag and YBCO also limit the use of this substrate. In addition, Ag is rather expensive from the aspect of mass production of the coated conductor. Ag without alloying elements is difficult to be

handled because it is mechanically soft. Thus, Ag/Ni and Ag/ Ni-alloys were used as these composite tapes are mechanically more robust.

Ni is one of the examples of FCC material that can be textured by rolling and crystallization to form an extremely sharp cube texture corresponding to (100)  $\langle 001 \rangle$ . However similar to Ag, pure Ni is relatively soft and defects can be easily formed on the surface of substrate. Besides, Ni is a ferromagnetic material that would encounter AC losses at 77 K. To overcome these problems, Ni alloys were studied. Ni alloys manage to reduce the magnetism and they are more mechanically robust. Examples of the Ni alloys are Ni-Cr, Ni-V, Ni-W, Ni-Fe and Ni-Cu (Huhne *et al.*, 2010, Thompson *et al.*, 2002). One of the main problems with the Ni alloyed with Fe and Cu is the corrosion problem of Cu and Fe as well as ferromagnetic properties of Ni-Fe. Research works is ongoing on the ternary Ni-based alloys for the optimization of the usage of Ni-based RABiT substrates such as Ni-Cr-W and Ni-Cr-V. Alloying elements such as Cr and V were proved to have improved mechanical and magnetic properties without causing any deterioration in texture (Boer *et al.*, 2001). W in Ni can also enhance the thermal stability of the pure Ni and restricted grain growth by strengthening the grain boundary of Ni-W. Besides, W in Ni is also known to have reduced  $T_c$  and reduced hysteresis (Kim *et al.*, 2006). Table 2.3 shows the example of different types of Ni-based alloy which have been development in consideration of mechanical and magnetic properties.

In recent year, Cu tapes have been researched as an alternative substrate. Compared to Ni and its alloys, Cu and its alloys have lower cost, easily developed cube texture, higher thermal conductivity, less chemical reactivity with YBCO and

they are non ferromagnetic. Diamagnetic Cu and its alloys have a very weak and negative susceptibility to magnetic fields. They are slightly repelled by a magnetic field and the material does not retain the magnetic properties when the external field is removed. However, Cu and Cu alloys are not resistant to oxidation at high temperatures in an ambient atmosphere (Kim *et al.*, 2007).

Table 2.3: Properties of some commonly used metallic RABiT substrates.

<b>Metallic substrate</b>	<b>Lattice constant (Å)</b>	<b>Transition temperature (K)</b>	<b>Coefficient of thermal expansion (<math>10^{-6}/^{\circ}\text{C}</math>)</b>	<b>Yield strength (MPa)</b>	<b>Melting point (<math>^{\circ}\text{C}</math>)</b>
Ag	4.07	0	17	70	961
Cu	3.62	0	13-17.4	75-344	1083
Ni	3.52	627	13	~ 30	1455
Ni-7at%Cr	3.54	250	11	75	~1430
Ni-9at%Cr	~3.54	124	-	59	~1430
Ni-11at%Cr	~3.54	20	-	64	~1430
Ni-13at%Cr	~3.54	0	-	87	~1430
Ni-9% V	3.52	-	11	102	~1425
Ni-50%Fe	3.59	-	~12	157*	~1450
Ni-5% W	~3.55	33	-	254*	-
Ni-3% W-2%Fe	-	-	12.9	183*	-

Keys: values at room temperature unless otherwise stated;

\*: denotes values at 76K .

### 2.5.3 Ion-Beam-Assisted Deposition (IBAD) Process

The IBAD process differs from the RABiT process in that no texture is forced on the starting metal strip. IBAD approach prepares the biaxially textured buffer layer by direct deposition of textured buffer layers on non-textured substrates. This is accomplished by using an ion beam impinging on the thin film buffer surface as it is being laid down in a vapour phase deposition. The impinging ions from the ion beam selectively cause re-emission of particles from the growing surface which has a certain alignment. Figure 2.7 shows the schematic illustration of IBAD process. Thus, in the IBAD process, the required surface texture results from the initial buffer



layer deposition rather than using the metal surface as an initial growth template. As comparison, the IBAD process is an extremely slow and expensive process than RABiTS process.

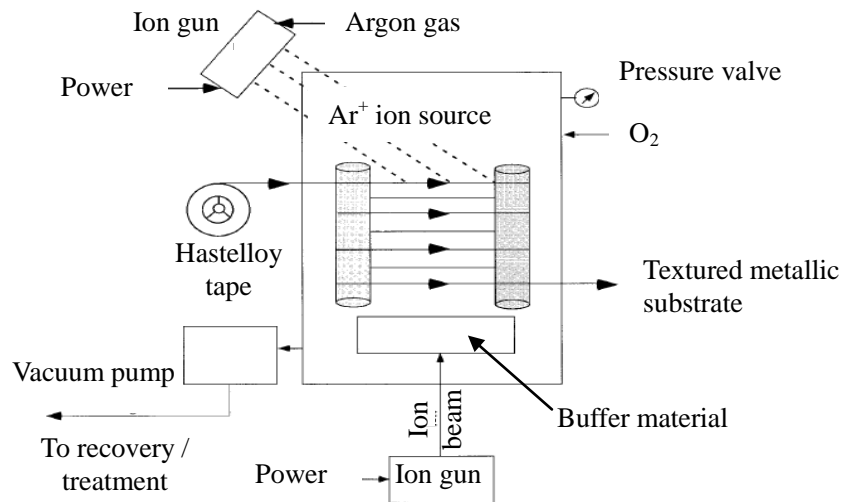


Figure 2.7: Schematic illustration of IBAD process (Sheth *et al.*, 1998).

#### 2.5.4 Inclined Substrate Deposition (ISD) Process

Similar to IBAD process, in ISD, the texture is made by texturing the buffer layer. Figure 2.8 shows the schematic illustration of ISD process. By inclining the substrate to the precise angle ( $\alpha$ ) with respect to the substrate, the buffer material is evaporated and formed the textured buffer layer on the substrate. ISD process is a much simpler approach and can be performed at a faster deposition rate than that in the IBAD process because it has no need of ion beam assistance (Ma *et al.*, 2002).

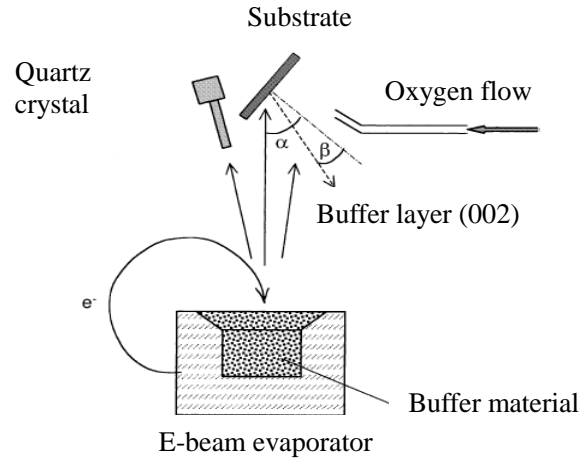


Figure 2.8: Schematic illustration of ISD process (Ma *et al.*, 2002).

## 2.6 Oxide Buffer Layer

In the YBCO 2G wire technology, buffer layer serves several important purposes: (i) to act as a chemical barrier to prevent diffusion of metallic elements into YBCO layer; (ii) to prevent the oxidation of the metallic substrate during the YBCO processing at high temperatures in an oxygen atmosphere; and (iii) to transmit the texture from the substrate to YBCO layer (Yang *et al.*, 2009, Driessche *et al.*, 2005). To be used as a good buffer layer for YBCO coated conductor application, the buffer layer must have a smooth, textured and crack free surface. As now the 2G wires are entering market place, cost effective and simple methods of buffer layer deposition is highly sought after. The various deposition techniques of oxide buffer layer are discussed as follow.

### 2.6.1 Buffer Layer Deposition Techniques

The available options to form buffer layer on a metallic substrates can be divided into: physical methods (vacuum) and chemical methods (non-vacuum). Examples of physical methods are pulsed laser deposition (PLD), evaporation,

sputtering and molecular beam epitaxy. On the other hand, chemical methods involve chemical solution deposition (CSD), chemical vapour deposition (CVD), electrochemical deposition and liquid phase epitaxy (LPE). The deposition techniques and the definition of the respective techniques are listed in Table 2.4.

Table 2.4: Buffer layer deposition methods and their respective definition.

<b>Deposition method</b>	<b>Definition</b>
<b>Pulsed laser deposition (PLD)</b>	Pulsed laser beam is focused to the target material in vacuum. The vaporization of material creates plasma plume which deposits the material on the surface of the substrate.
<b>Evaporation deposition</b>	The source material is evaporated in vacuum done by thermal source or electron beam. The vapour particles then travel directly to the substrate and condense back to solid state.
<b>Sputtering deposition</b>	Bombardment of the target material by energetic particles and the ejection of the particles from target are deposited on the substrate.
<b>Molecular beam epitaxy (MBE)</b>	The individual components that form the film are evaporated from separated sources. The evaporation sources may be electron beam-heated or conventional resistance-heated effusion. Activated oxygen or ozone is applied to the substrate to compensate for the low reactive gas pressure permitted.
<b>Chemical solution deposition (CSD)</b>	The process starts with the preparation of precursor solution and followed by deposition of the coating solution on the substrate by spin coating, spray coating or dip coating in the solution. Subsequently, the as-deposited film is dried, pyrolyzed, crystallized, and post-annealed (optionally) for densification or phase transformation.
<b>Chemical vapour deposition (CVD)</b>	The volatile starting materials are heated to form vapours. The materials are mixed at suitable temperature and then transport to the substrate surface by using carrier gas. The solid product is crystallised out.
<b>Electrochemical deposition</b>	The process involves chemical redox process where an electrical potential is applied between a conducting area on the substrate and a counter electrode (usually platinum) in the electrolyte, resulting in the formation of a coating on the substrate. This process usually generates some gas at the counter electrode.

Table 2.4: Buffer layer deposition methods and their respective definition (*cont.*).

<p><b>Liquid phase epitaxy (LPE)</b></p>	<p>The solution is kept in the LPE furnace at melting temperature with continuous stirring. Then the temperature is slowly lowered to the supersaturation temperature at which point the substrate is dipped in the solution. The substrate is rotated at a constant rate to facilitate homogeneous growth of the film. Finally the substrate is removed from the solution and then spun in furnace to remove the residual flux.</p>
--	--

In recent years, a lot of works have been done on the study of the formation of oxide buffer layer for superconductor applications. This includes the study of the process formation of the thin film and the thin film material itself. Table 2.5 shows several typical physical and chemical methods used to deposit several examples of buffer layer oxides from 2005 to 2010. Note that prior to 2005, most works were geared at the formation of simple binary oxide for buffer layer and/or the formation of multi layered binary oxides via physical deposition method.

Nonetheless, from Table 2.5, it could be seen that most authors have reached a consensus by stating that chemical methods are much preferred due to the cost effectiveness of the methods. Chemical methods through CSD process has been proven to be the most viable low-cost, non-vacuum method which could be adopted for high volume manufacturing enabling the commercialisation of 2G YBCO based superconductor cables. CSD is indeed an inexpensive process since it does not require vacuum equipment. Apart from that, by controlling the process chemistry, the oxide produced would be of high quality.